

Ocean response to arbitrary wind perturbations in the low-frequency approximation: implications for ENSO and decadal climate variability

Melanie Parker^{a*} and Alexey Fedorov^a

melanie.parker@yale.edu, alexey.fedorov@yale.edu

^aYale University Department of Geology and Geophysics
210 Whitney Avenue New Haven, CT 06511

*Corresponding Author

Tel: 001 203 432-3159

Fax: 001 203 432-3134

Abstract

We study the response of the ocean thermocline in the Pacific to arbitrary periodic wind stress perturbations in the low-frequency limit. This approximation assumes that the characteristic period of the wind forcing is much longer than the propagation timescales of the first-order baroclinic waves involved in ocean adjustment. Starting from the reduced-gravity 1½-layer model and building on the recent results of Fedorov (2010), we obtain solutions of the forced shallow-water equations in terms of a perturbation expansion about a small parameter that involves the dominant frequency of the wind forcing and the oceanic damping rate. This expansion parameter is roughly proportional to the ratio of the time necessary for equatorial Kelvin waves to cross the Pacific Ocean to the characteristic period of the forcing, which is much smaller than unity for climate variations with interannual and longer timescales. We use the obtained analytical expressions to examine different idealized cases relevant to El Niño/Southern Oscillation (ENSO) and decadal climate variability in the Pacific, such as periodic variations of the zonal wind stress in the equatorial band, variations of the meridional wind stress in the vicinity of the eastern boundary of the basin, and wind stress variations in mid-latitudes. In particular, we focus on the details of the ocean response to these wind perturbations in the eastern equatorial Pacific and the region along the California coast. We compare the results obtained from the low-frequency approximation with those from the 1½-layer model and find a good agreement even for periods of oscillations longer than 1-2 years. Using the low-frequency approach we derive a number of simple analytical expressions, including expressions for the offshore decay scale of thermocline anomalies at the basin eastern boundary and the phase lag between variations in the mean thermocline depth along the equator and the Niño3 SST. Ultimately, the results of this study demonstrate that the low-frequency limit provides a useful tool for modeling ENSO and decadal climate variability.

Keywords: ENSO, ocean thermocline, ocean thermal structure, equatorial oceanography, coastal upwelling

1 Introduction

Climate variability in the Pacific Ocean is dominated by interannual and, to a somewhat lesser extent, decadal timescales. Typically, this variability involves changes in surface wind stress that result in ocean adjustment that involves changes in the depth of the ocean thermocline. The obvious examples are El Niño/Southern Oscillation (ENSO), the Pacific Decadal Oscillation (PDO), and the North Pacific Gyre Oscillation (NPGO). ENSO is known to be the primary mode of variability in sea surface temperature in the equatorial Pacific, as well as the dominant mode of variability overall in the Pacific which influences climate and weather patterns worldwide (e.g. Lluich-Cota et al. 2003). The PDO is thought to be the primary mode of decadal variability with a pronounced signature in SSTs especially in the Northern Pacific (e.g. Mantua and Hare 2002). NPGO is another mode of decadal variability (corresponding to the second EOF), which has a strong signature in variations of sea surface salinity, nutrients and chlorophyll especially in the Northeast Pacific (e.g. Di Lorenzo et al. 2008).

The dynamics of ENSO, associated with ocean-atmosphere coupling in the equatorial region, have been extensively studied (e.g. Philander 1990). The mean state of the equatorial Pacific is characterized by easterly trade winds, which cause the thermocline to be deeper in the west with warmer surface waters. The thermocline is shallow in the east, allowing cold water to be upwelled to the surface. During an El Niño event, for example, the trade winds weaken which excites a host of equatorial downwelling Kelvin waves. These waves propagate eastward pushing the thermocline deeper in the east, and reducing the thermocline slope across the equatorial Pacific. When the Kelvin waves reach the western coast of the Americas, coastal Kelvin waves travel north and south along the coast.

The subsequent, longer-term ocean adjustment of the broader Pacific involves westward propagating baroclinic Rossby waves excited by the coastal Kelvin waves (Clarke and Dottori 2008). In fact, changes in sea surface height (SSH) observed during and after El Niño events along the California coast (Figure 1) are largely due to these Rossby waves (e.g. Jacobs et al. 1994) rather than the initial Kelvin waves. These Rossby waves can carry the signal relatively far offshore (by some 20° of longitude or more, Figure 1), whereas Kelvin wave amplitude decays quickly over one baroclinic Rossby radius of deformation (~20-30km) away from the coast.

These SSH anomalies reflect changes in the thermocline depth during the ENSO cycle and decadal climate variations. SSH anomalies increase in the Niño3 region as a result of equatorial Kelvin wave propagation during an El Niño event (Figure 1a). Baroclinic Rossby waves then propagate westward from the coast of North America, causing an SSH signal along this coastal region (Figure 1b). As these Rossby waves propagate westward, an SSH signal is visible offshore as far as 20-30° (Figure 1c and 1d). Most of these changes are a combination of direct and indirect response of the broader tropical Pacific Ocean to wind variations.

Similarly, many aspects of decadal climate variability in the Pacific Ocean can be attributed to changes in wind stress, especially over the North Pacific. For example, Mantua and Hare (2002) found changes in this wind stress force oceanic modifications, including altering the strength of the gyre circulation and meridional SST gradients. They argue that this transient response of the ocean to changes in wind stress causes the phase shift seen in the decadal mode in the North Pacific and allows the system to oscillate.

A climate regime shift was also observed in the Pacific in 1976-77, resulting in changes in SSTs and sea level pressure (SLP) (e.g. Nitta and Yamada 1989, Hare and Mantua 2000). The observed decadal changes in wind stress as well as wind-driven upper ocean mixing and Ekman processes were found to have a basin-wide spatial pattern consistent with the observed changes in SST across the regime shift. Higher wind stress and colder SSTs were observed in the region of the North Pacific Current, with lower wind stress and warmer SSTs at higher and lower latitudes (Parrish et al., 2000).

Locally, surface wind stress also affects upwelling along the coast of California as part of the California Current System. Alongshore winds directed toward the equator cause surface waters to move away from the coast as a result of Ekman transport. Cold water is then upwelled to replace the water that has moved offshore. This system is composed of a southward current that extends from off the coast of Oregon to Baja, California and reaches 1000km offshore (Miller et al. 1999). The upwelling produces a region of cold, nutrient-rich water along the coast of California, which is critical to the marine ecosystem (Miller et al. 1999). Upwelling in this region is affected by variations in the local ocean thermal structure, such as variations in the depth of the thermocline. Subsurface thermal anomalies can be forced along the coast of North America either by propagation of thermocline anomalies initially forced in the eastern equatorial Pacific Ocean, or by variations in the local wind stress caused either by atmospheric teleconnections from ENSO (Lluch-Cota et al. 2003; Subbotina et al. 2001; Huyer et al. 2002) or wind forcing from the NPGO (e.g. DiLorenzo et al. 2008).

Several studies have explored the effects of local versus remote forcing of this region by El Niño events. Hermann et al. (2009) found the largest combined response of the 1997-1998 El Niño (local and remote forcing) in the coastal Gulf of Alaska with smaller effects in the California Current System, indicating a large local response in the coastal Gulf of Alaska. Meyers et al. (1996) and Pares-Sierra and O'Brien (1989) used a reduced-gravity model to investigate the effects of local wind stress variations on the Northeast Pacific versus remote forcing via coastal Kelvin waves.

Forcing the model initially with local wind stress, Meyers et al. (1996) found that oceanic variability in the Northeast Pacific was dominated by changes in large-scale gyre circulation. When they induced equatorial Kelvin waves in the model, westward propagating Rossby waves were excited along the coast of North America, which acted to change the depth of the thermocline offshore. Also, they noted that high-frequency variations were forced locally whereas longer-term variations resulted from remote forcing via the coastal Kelvin waves. Pares-Sierra and O'Brien (1989) concluded that sea

level anomalies along the coast of California are primarily driven by remote forcing from the equatorial region. Strub and James (2002) used altimeter data to investigate variations in SSH during the 1997-1998 El Niño. They found symmetry in the coastal SSH patterns between the Northern and Southern hemispheres which extended to 15°S and 20°N. At higher latitudes this symmetry diminished, indicating an effect of the local wind stress.

In summary, the response of the Pacific Ocean to wind variations on interannual to decadal timescales includes both local and remote effects of wind stress on the ocean thermocline. To describe this response in simple and intermediate models the reduced-gravity shallow water equations are typically used (e.g. Battisti 1998). The goal of this study is relatively modest – to obtain, in an idealized setting, a general analytical solution of the shallow water equations for thermocline depth anomalies in the Pacific Ocean relevant to the aforementioned aspects of ocean adjustment. Using this solution, we will explore several particular cases – from zonal wind stress anomalies in the western Pacific to zonal anomalies in the mid-latitudes, to meridional anomalies off the coast of North America.

The low-frequency model allows us to solve the shallow-water equations without an explicit representation of Kelvin and Rossby waves using a perturbation expansion. Building on the method of Fedorov (2010), here we will solve the shallow-water equations for wind stress variations of an arbitrary spatial structure. The method is referred to as a “low-frequency approximation” due to the small frequency of ENSO and decadal climate variability compared to the timescale of equatorial wave propagation. For instance, ENSO has a periodicity of approximately three to six years, whereas the physical processes that control the dynamics of ENSO (Kelvin and Rossby wave propagation) have much shorter timescales. Kelvin waves cross the Pacific basin in about two months and equatorial Rossby waves cross the basin in about six months. In comparison to these processes, ENSO itself can be considered a low-frequency phenomenon. A somewhat similar low-frequency approach to ENSO was also proposed by Clarke (2010).

The structure of this paper is as follows. In section 2 we discuss the 1½-layer shallow-water model and we then solve the equations for an arbitrary wind stress anomaly that can have both zonal and meridional components and can be located on or off of the equator. In section 3, we compare the results from the 1½-layer model to results from the low-frequency method for zonal wind stress anomalies and discuss implications for variations in the mean thermocline depth, related to variations in the warm water volume in the equatorial Pacific, as an application of the low-frequency method. In section 4, we compare the results from the 1½-layer model to results from the low-frequency method for meridional wind stress anomalies. Section 5 concludes the paper.

2 Method: the low-frequency expansion for the shallow-water equations

The objective of this study is to use the low-frequency approximation (Fedorov 2010) to solve the full shallow water equations using a perturbation expansion, and investigate the effects of several idealized wind stress anomalies on the depth of the thermocline in the Pacific.

We begin with the shallow water equations on the equatorial β -plane

$$u_t + g^* h_x - \beta y v = \frac{\tau^{(x)}}{\rho H} - \varepsilon_m u \quad (1)$$

$$g^* h_y + \beta y u = \frac{\tau^{(y)}}{\rho H} \quad (2)$$

$$h_t + H(u_x + v_y) = -\varepsilon_m h \quad (3)$$

Here, x , y and t denote zonal coordinate, meridional coordinate and time, and the subscripts stand for the corresponding derivatives. H and $h=h(x,y,t)$ are the mean and anomalous thermocline depths respectively. u and v are the zonal and meridional velocities, ε_m is ocean damping, and $g^* = g \frac{\Delta\rho}{\rho}$ is the reduced gravity, with ρ the water density above the thermocline and $\Delta\rho$ the change in water density over the thermocline. The two-dimensional field of wind stress anomalies is represented by τ , where $\tau^{(x)}$ and $\tau^{(y)}$ are the zonal and meridional components of the applied wind stress.

We approximate the Pacific as a rectangular basin with the western boundary located at 130°E , representing the western Pacific along Indonesia and Australia. The basin extends eastward 150° with the eastern boundary representing the western coasts of North and South America. The no-flow condition is applied along the eastern boundary ($u|_{x=280^\circ\text{E}} = 0$) and the no-net-flow condition is applied along the western boundary ($\int_{-\infty}^{\infty} u|_{x=130^\circ\text{E}} dy = 0$).

For simplicity, the meridional acceleration term (v_t) in these equations is neglected, which is a good approximation for slow motions. In such an approach, the thermocline depth changes instantaneously along the eastern boundary of the model basin (and within the Rossby radius of deformation from the coast). This is consistent with the fact that coastal Kelvin waves travel much faster than the timescales of the slow motion to be considered. Whether we retain or not the meridional acceleration does not affect the leading order expansion term in the low-frequency approximation.

Typically, equations (1)-(3) are expanded into a set of orthogonal Hermite functions that describe the eastward propagating equatorial Kelvin waves and the westward propagating equatorial Rossby modes (see Battisti 1998 for details). Also note that the equatorial β -plane approximation is quite accurate not only in the tropics but also in mid-latitudes. In

fact, this approximation gives only a 13% error for the Coriolis parameter at 50°N or 50°S. This allows us to use this approximation for mid-latitude wind stress anomalies.

Next, we nondimensionalize equations (1)-(3) using several characteristic scales: the zonal coordinate is scaled by the basin width L , and the meridional coordinate is scaled

by the Rossby radius $L_R = \left(\frac{c_0}{\beta}\right)^{1/2}$, where c_0 is the speed of a Kelvin wave. Time is scaled

by the time required for a Kelvin wave to cross the basin $T_K = \frac{L_R}{c_0}$. After

nondimensionalization, equations (1)-(3) can be written as

$$\hat{u}_{\hat{t}} - \hat{y}\hat{v} = -\hat{h}_{\hat{x}} - \hat{\varepsilon}_m \hat{u} + \hat{\tau}^{(x)} \quad (4)$$

$$\hat{y}\hat{v} = -\hat{h}_{\hat{y}} + \hat{\tau}^{(y)} \quad (5)$$

$$\hat{h}_{\hat{t}} + \hat{u}_{\hat{x}} + \hat{v}_{\hat{y}} = -\hat{\varepsilon}_m \hat{h} \quad (6)$$

where $\varepsilon_m = (L/c_0)\varepsilon_m$, $\hat{\tau}^{(x)} = (L/\rho H c_0^2)\tau^{(x)}$, and $\hat{\tau}^{(y)} = (L_R/\rho H c_0^2)\tau^{(y)}$. A Fourier transform is then applied to u , v , h and τ . The resulting equations (using the same notations as those used for the original variables) are

$$h_x - yv = \tau^{(x)} - \varepsilon u \quad (7)$$

$$h_x - yv = \tau^{(y)} \quad (8)$$

$$u_x + v_y = -\varepsilon h \quad (9)$$

where $\varepsilon = \varepsilon_m + i\omega$.

Simple algebra yields a vorticity equation for this system

$$v = \tau_x^{(y)} - \tau_y^{(x)} + \varepsilon u_y + \varepsilon y h \quad (10)$$

Equations (7)-(9) can be rewritten as

$$h_x - y^2 \varepsilon h = \tau^{(x)} + y(\tau_x^{(y)} - \tau_y^{(x)}) + \varepsilon(yu_y - u) \quad (11)$$

$$u = \frac{1}{y}(\tau^{(y)} - h_y) \quad (12)$$

The perturbation expansion used in this method involves a small parameter $\varepsilon = \varepsilon_m + i\omega$ where ε_m is the ocean damping and ω is the frequency of the wind forcing (a typical realistic ocean damping timescale of two years results in a non-dimensional ε_m value of 0.1). Formally we will require that $|\varepsilon| \ll 1$, which is true for oscillation periods sufficiently longer than one year (Figure 2). In practice, the approximation will work well for periods longer than two years.

We now expand h in powers of ε , assuming $|\varepsilon|$ is a small parameter, as $h = h^{(0)} + \varepsilon h^{(1)} + \varepsilon^2 h^{(2)} + \dots$ and apply this expansion to equation (11) to obtain the expression for the zeroth order solution, $h^{(0)}$

$$h_x^{(0)} - y^2 \varepsilon h^{(0)} = \tau^{(x)} + y \left(\tau_x^{(y)} - \tau_y^{(x)} \right) \quad (13)$$

It is important for this approach to keep the second term on the left-hand-side of equation (13), since it can become large for large $|y|$ and reach the same order as the first term.

Using the boundary condition at the eastern boundary ($u|_{x=280^\circ E} = 0$) and equation (13),

$$h^{(0)} = e^{\varepsilon y^2 (x-1)} \left[\int_0^y \tau^{(y),E} dy - y \tau^{(y),E} + M \right] + y \tau^{(y)} - e^{\varepsilon y^2 x} \left[\int_x^1 e^{-\varepsilon y^2 s} \left(\tau^{(x)} - y \tau_y^{(x)} \right) ds \right] - \varepsilon y^3 \int_x^1 \tau^{(y)} e^{\varepsilon y^2 (x-s)} ds \quad (14)$$

The value of the constant M is found using the boundary condition at the western boundary ($\int_{-\infty}^{\infty} u|_{x=130^\circ E} dy = 0$) and equation (12) for u

$$M = \sqrt{\frac{\varepsilon}{\pi}} \left[\int_{-\infty}^{\infty} \int_0^1 \left(s \tau^{(x)} - \frac{1}{2} y \tau^{(y)} \right) e^{-\varepsilon y^2 s} ds dy - \int_{-\infty}^{\infty} e^{-\varepsilon y^2} \left(\int_0^y \tau^{(y),E} d\tilde{y} \right) dy \right] \quad (15)$$

Here, $\tau^{(y),E}$ is the meridional component of the wind along the eastern boundary of the basin ($x=280^\circ E$).

Expressions (14) and (15) allow us to obtain solutions for oscillatory wind stress forcing of an arbitrary shape. If the wind stress forcing is sinusoidal, then one would simply multiply (14) with $e^{i\omega t}$ and then take real or imaginary part of the expression to obtain the spatial pattern of the oscillation at different phases.

Next, we consider three particular cases relevant to ENSO and decadal climate variability in the Pacific: periodic variations of the zonal wind stress in the equatorial band, variations of the coastal wind stress along the eastern boundary of the basin, and variations of the extra-tropical wind stress in mid-latitudes.

3 Results: zonal wind stress

We investigate two types of zonal wind stress anomalies: an equatorial anomaly and a mid-latitude anomaly. The equatorial wind stress anomaly is analogous to ENSO-like wind variations in the equatorial Pacific on interannual timescales. The mid-latitude wind stress anomaly is relevant to decadal climate variability in mid-latitudes as discussed, for example, in Deser et al. (1996), who suggest that observed changes in the mixed layer depth between 1970 and 1991 in the northern central Pacific Ocean may be caused, in part, by changes in surface wind forcing. The low-frequency method allows us to apply mid-latitude periodic wind stress anomalies and track the resulting thermocline

depth anomalies in the basin. Using equation (14), we derive a general expression for thermocline depth anomalies resulting from an applied zonal wind stress anomaly and then compare the results to the 1½-layer model forced by the same wind stress anomalies.

3.1 Equatorial zonal wind stress

The first idealized case we examine is a periodic variation in the zonal wind stress along the equator (reminiscent of wind variations associated with ENSO). We apply a wind stress anomaly with a sinusoidal dependence and a period P . The wind stress for this case is of the form $\tau^{(x)} = Ae^{-\alpha(y-y_c)^2} e^{-\gamma(x-x_c)^2} e^{i\omega t}$ with $\tau^{(y)} = 0$ (Figure 3a). This is a conventional representation of wind stress in simple ENSO models (e.g. Jin and Neelin 1993), and the proportionality coefficient A is computed from a regression of the wind stress onto Niño3 SSTs. After calculations, the real or imaginary part of the expressions will give actual thermocline anomalies.

Without meridional winds equation (14) becomes

$$h^{(0)} = Me^{\varepsilon y^2(x-1)} - \int_x^1 e^{\varepsilon y^2(x-s)} (\tau - y\tau_y) ds. \quad (16)$$

Substituting the expression for the applied equatorial wind stress, we rewrite equation (16) as

$$h^{(0)} = Me^{\varepsilon y^2(x-1)} - e^{\varepsilon y^2 x} (1 + 2\alpha y^2) e^{-\alpha y^2} \int_x^1 \tau(s) e^{-\varepsilon y^2 s} ds \quad (17)$$

where $M = \int_0^1 x\tau(x) \sqrt{\frac{\varepsilon}{\varepsilon x + \alpha}} dx$ and $\tau(s) = \tau(x, y)|_{x=s, y=0}$ is the wind stress along the equator.

In this expression, M has a sense of the thermocline depth anomaly along the eastern boundary of the basin. Previously, this case was examined in part by Fedorov (2010) and our general formula for thermocline depth anomalies reduces to a similar expression as in their study.

Thermocline depth anomalies forced by the applied wind stress and obtained from the low-frequency expression reveal spatial patterns (Figure 4) familiar from ENSO studies (e.g. Schwing et al. 2002). Figure 4a shows an El Niño-like state in the Pacific and Figure 4c shows thermocline anomalies preceding (by a quarter-period) an El Niño event. During the El Niño event, the surface wind anomalies are directed towards the east, which causes the thermocline to deepen in the eastern equatorial region of the basin. The thermocline shoals in the western equatorial region off the equator as the warm surface waters move across the basin. One quarter-period prior to the El Niño event, the thermocline anomalies are strongest off the equator. At the same time, the equatorial thermocline deepens everywhere along the equator, increasing the ocean heat content along the equator and recharging the ocean for the following El Niño event.

We compare these results to results from the 1½-layer model forced with the same wind stress over a similar model basin (Figure 4b and 4d). The comparison shows a very good quantitative agreement between the 1½-layer model and our low-frequency results, including similar anomaly spatial structures and anomaly amplitudes.

The normalized root mean squared error was also calculated to compare the results from the low-frequency method to results from the 1½-layer model. The error was calculated as $[\int \int (h_{1.5} - h_{lf})^2 dx dy]^{1/2} [\int \int (h_{1.5})^2 dx dy]^{-1/2}$ for periods of the wind forcing ranging from one to ten years (Figure 5, solid line). The error is less than 40% for the 2-year period and quickly decreases for longer periods.

It is also instructive to use the derived expression for thermocline depth anomalies to investigate the decay scale of the thermocline anomalies away from the eastern boundary. As the signal is carried offshore by Rossby waves, the magnitude of the thermocline depth anomaly will decrease due to ocean damping of the waves. The narrowing of the anomaly along the eastern boundary of the basin is due to the decrease in the Rossby wave speed away from the equator.

It is important that the second term in (17) vanishes sufficiently far away from the wind stress anomaly, so that the first term solely determines the behavior of the solution near the eastern boundary. Therefore, the exponential factor $e^{\varepsilon_m y^2 (x-1)}$ describes the offshore decay and gives the offshore e-folding decay scale as

$$D_{OS} = \frac{1}{y^2 \varepsilon_m} \quad (18)$$

where y is latitude in meters. For instance, at 25°N, we obtain a dimensional value of $D_{OS} = 22.5^\circ$.

This scale is controlled by the Rossby waves that carry the signal westward from the eastern boundary and by oceanic damping. We can easily estimate this scale using the physics of these waves. The phase speed of long mid-latitude Rossby waves is $c = -\beta L_R^2$ where L_R is the internal Rossby radius of deformation (not equatorial). L_R is inversely proportional to the Coriolis parameter f . Therefore, in the β -plane approximation the spatial decay scale should be inversely proportional to y^2 in full agreement with (18).

We further compare the decay scale from the low-frequency method to the decay scale from the 1½-layer model results. Thermocline depth anomalies from the 1½-layer model for an applied equatorial wind stress with period ranging from one to ten years were used to estimate the decay scale (Figure 6a, solid line). Decay scales were also calculated for the low-frequency method results (Figure 6a, dashed line). The decay scales for both methods approach the value calculated above from equation (18), showing a good agreement for longer-period wind stress anomalies. For shorter periods, on the order of 1-2 years, the decay scale is slightly shorter than predicted by the low-frequency approach.

3.2 Mid-latitude zonal wind stress

Next, we apply a wind stress of the same shape and structure as was used in the equatorial wind case ($\tau^{(x)} = Ae^{-\alpha(y-y_c)^2}e^{-\gamma(x-x_c)^2}e^{i\omega t}$ with $\tau^{(y)} = 0$) but shift it north of the equator in increments of ten degrees. We are able to use equation (17) here but change the value of y_c in the wind expression (meridional center of the wind stress) in order to move the wind stress meridionally. We look at three cases: wind stress centered at 10°N, 20°N and 30°N (Figure 7, left column) and use the forcing period $P=10$ years. The effect of westerly wind stress anomalies is a deepening of the thermocline south of the maximum wind stress and shoaling of the thermocline north of the maximum wind stress (Figure 7, middle column). The comparison of these results to those from the 1½-layer model is nearly perfect (Figure 7, right column).

When the wind stress anomaly is centered at 10°N, the thermocline anomaly still resembles that during El Niño, except for the missing off-equatorial lobe in the Northern hemisphere. However, when the wind stress is moved far away from the equator, the equatorial thermocline is barely affected and the ocean response is largely confined to the vicinity of the winds, in agreement with the results of Emile-Geay and Cane (2009).

We can use the low-frequency results to investigate in more detail how the thermocline depth at the eastern boundary varies with the period of the applied wind stress and its distance from the equator (Figure 8a). The thermocline anomaly at the eastern boundary is clearly largest when the wind is centered on the equator. However, as the zonal wind stress is moved north (or south) of the equator, the impact of the oscillation period changes: whereas for equatorial winds the thermocline depth anomaly at the eastern boundary decreases with longer periods, it increases for mid-latitude winds. The latter effect is apparently related to ocean adjustment that involves Rossby wave propagation in the mid-latitudes.

3.3 Mean thermocline depth and eastern equatorial SSTs

We are also able to use the low-frequency approximation to derive an explicit expression for the phase lag between variations in the mean depth of the equatorial thermocline (averaged across the basin) and eastern equatorial SSTs. In observations the mean thermocline depth is often related to ocean heat content (OHC) or to the warm water volume (WWV) of the equatorial ocean. Variations in these variables – OHC, WWV and the mean thermocline depth – are highly correlated. In the idealized model we use the mean thermocline depth to represent the other two.

Variations in the WWV of the equatorial Pacific are an important element of the recharge-discharge paradigm of ENSO dynamics (Jin 1997, Meinen and McPhaden 2000, also see Fedorov and Brown 2009). Observations show that variations in equatorial WWV lead variations in eastern equatorial Pacific SSTs by approximately 6 months to 1 year. Our results from the low-frequency method (Figure 4d, showing a nearly uniform deepening of the equatorial thermocline preceding an El Niño event) are generally

consistent with these observations (in our study the mean depth of the thermocline along the equator represents WWV).

We begin with equation (16), substitute the expression for the equatorial wind stress anomaly, and derive an expression for the phase lag between WWV and eastern equatorial SSTs. This method follows Fedorov (2010); however here we also consider the effect of shifting the wind stress anomaly off the equator.

From (16), the thermocline depth along the equator is calculated as

$$h(x) = e^{-\frac{\alpha y_c^2 \varepsilon x_c}{\varepsilon x_c + \alpha}} \sqrt{\frac{\varepsilon}{\varepsilon x_c + \alpha}} \int_0^1 x \tau(x) dx - e^{-\alpha y_c^2} \int_x^1 \tau(s) ds. \quad (19)$$

The mean depth of the equatorial thermocline is defined as

$$h_m = \int_0^1 h^{(0)} dx. \quad (20)$$

The subscript m denotes averaging over the entire length of the basin versus averaging over the eastern equatorial Pacific (subscript e). We now obtain

$$h_m = e^{-\alpha y_c^2} \left(e^{\frac{\alpha^2 y_c^2}{\varepsilon x_c + \alpha}} \sqrt{\frac{\varepsilon}{\varepsilon x_c + \alpha}} - 1 \right) \int_0^1 x \tau(x) dx. \quad (21)$$

Let us now assume that wind stress anomalies along the equator are proportional to T_e (averaged SST in the eastern equatorial Pacific).

$$\tau(x) = A e^{-\frac{\alpha(y-y_c)^2}{2}} e^{-\gamma(x-x_c)^2} e^{i\omega t} T_e \quad (22)$$

Now the equation for the mean thermocline depth (21) can be rewritten as

$$T_e = h_m e^{\alpha y_c^2} \left(e^{\frac{\alpha^2 y_c^2}{\varepsilon x_c + \alpha}} \sqrt{\frac{\varepsilon}{\varepsilon x_c + \alpha}} - 1 \right)^{-1} \left(A \int_0^1 x e^{-\gamma(x-x_c)^2} dx \right)^{-1}. \quad (23)$$

Since $\varepsilon = \varepsilon_m + i\omega$ is a complex number this expression implies that there is a lag between the mean thermocline depth and temperature in the east

$$\phi = -\text{arg} \left(e^{\frac{\alpha^2 y_c^2}{(\varepsilon_m + i\omega)x_c + \alpha}} \sqrt{\frac{\varepsilon_m + i\omega}{(\varepsilon_m + i\omega)x_c + \alpha}} - 1 \right). \quad (24)$$

Negative ϕ here would mean that variations in temperature lag those in the thermocline depth. This expression reduces to the phase lag derived by Fedorov (2010) for $y_c=0$ (that is when the wind stress anomaly is centered exactly on the equator).

We can now consider how shifts in the position of the wind stress anomaly away from the

equator affect the lag. For further calculations we use realistic values of $\alpha=0.12$ (which corresponds to a meridional e-folding decay scale of the wind stress of about 9°) and $\varepsilon_m=0.1$ (corresponding to an ocean damping rate of 2 years^{-1}). Figure 9 shows how the phase lag changes with oscillation period for several values of y_c . Negative phase lag values indicate that T_e lags h_m . When the wind stress anomaly is centered on the equator, T_e lags h_m by approximately 8 months for an oscillation period of 4 years.

Even a few-degree shift of the wind anomaly reduces the absolute value of the phase lag drastically. When the center of the wind stress is located farther than 7° away from the equator, we see a reversal in the phase lag behavior with variations in T_e now leading h_m on interannual and decadal timescales. This happens because when the wind anomaly is shifted sufficiently far from the equator, there is little influence of winds directly along the equator. As a result, any variations in the eastern equatorial SSTs are forced remotely via Rossby waves travelling westward and reflecting from the western boundary, and not by Kelvin waves, so that the phase lag does not reflect the usual ENSO dynamics any longer.

We can also consider the effect on the phase lag of changing the meridional extent of the wind anomaly, which is proportional to $\alpha^{-1/2}$. Both parameters, y_c and α , determine the meridional shape of the wind stress. The values of the lag turn out to be quite sensitive to changes in these two parameters as well as the period of the forcing (Figure 10). For example, in a reasonable range of y_c and α , and for the oscillation period of 4 years, the phase lag ranges from roughly 20 to 100 degrees. Narrow wind anomalies centered at the equator (large α , $y_c=0$) produce the longest lag. For small values of y_c in a broad range of α , the phase lag remains negative (i.e. variations in the Niño3 SST lag those in the mean thermocline depth along the equator). Our calculations further confirm that for narrow wind anomalies shifted away from the equator the expected phase relationship breaks down yielding positive values of ϕ (Figure 10, upper right corner).

4 Results: meridional wind stress

As in the previous section, we consider two types of meridional wind stress anomalies: a coastal anomaly along the eastern boundary of the basin and an offshore anomaly, both in mid-latitudes (more exactly in the subtropics). Beginning from equation (14) we obtain an expression for thermocline depth anomalies induced by meridional wind stress variations, and compare the results to the $1\frac{1}{2}$ -layer model forced by similar wind stress anomalies. In the examples considered, the coastal wind forcing will vary on interannual timescales and the mid-latitude forcing on decadal timescales.

4.1 Coastal meridional wind stress

We apply a meridional wind stress anomaly centered at 25°N along the eastern boundary that undergoes sinusoidal variations, so that wind direction changes from northward to southward every half-period. This wind stress has the form $\tau(y) = Ae^{-\alpha(y-y_c)^2} e^{-\gamma(x-x_c)^2} e^{i\omega t}$ with $\tau(x) = 0$ (Figure 3b). As an example, we use wind forcing with a 4 year period, similar to the typical period of ENSO. It is commonly

observed that coastal, predominantly northerly winds blowing along the coast of North America relax during El Niño events as part of an atmospheric teleconnection mechanism typically referred to as the Pacific North American pattern (PNA). The goal of our calculations is to investigate the thermocline response to such wind variations in an idealized setting.

Substituting this wind stress into equation (14) yields thermocline depth anomalies as

$$h^{(0)} = e^{\varepsilon y^2(x-1)} \left[\int_0^y \tau^E dy - y\tau^E + M \right] + y\tau - y^3 \varepsilon \int_x^1 \tau(s) e^{\varepsilon y^2(x-s)} ds \quad (25)$$

where $\tau(s) = \tau(x, y)|_{x=s}$ and

$$M = \sqrt{\frac{\varepsilon}{\pi}} \int_{-\infty}^{\infty} \left[\left(\int_0^1 -\frac{1}{2} y \tau e^{-\varepsilon y^2 s} ds \right) - e^{-\varepsilon y^2} \left(\int_0^y \tau^E d\tilde{y} \right) \right] dy.$$

Here, we have used the fact that this wind stress forcing vanishes at the western boundary of the basin, i.e. $\tau^{(y),w} = 0$. Note that in contrast to the previous cases, the thermocline depth at the eastern boundary now varies with latitude.

Equation (25) gives a time varying solution of thermocline depth anomalies throughout the basin. Figure 11 shows the resultant ocean states when the wind stress anomaly is northward and maximum, and a quarter-period before that. When the wind stress is northward (Figure 11a), the thermocline deepens along the boundary as the anomalous Ekman transport causes surface waters to move towards the shore. There is a corresponding shoaling of the thermocline at some distance away from the coast caused by mass redistribution. A quarter-period before this state (Figure 11c), the wind stress anomaly is exactly zero, so that any observed thermocline depth anomalies were a result of transient ocean adjustment.

We again compare our low-frequency results to those from the 1½-layer model forced with the same wind stress and see very similar thermocline depth anomalies (Figure 11, right column).

We also calculate the normalized root mean squared error for the two models ($[\int \int (h_{1.5} - h_{1f})^2 dx dy]^{1/2} [\int \int (h_{1.5})^2 dx dy]^{-1/2}$, see Figure 5 dashed line). Similar to the case with the zonal equatorial wind stress forcing, we see a rapid decrease in the error as the frequency of the applied wind stress decreases (and its period increases). This is expected as the low-frequency method works best for lower frequencies.

Our results are also consistent with the study of Enriquez and Friehe (1995), who also used a 1½-layer model and studied how changes in wind stress curl modify coastal upwelling.

4.2 Offshore decay scale of thermocline depth anomaly

Wind stress anomalies along the basin eastern boundary affect the region offshore in two principle ways: wind stress modifies the ocean thermocline locally whereas Rossby waves carry the signal westward away from the area where the wind stress is applied. As

a result, the offshore effective decay scale is somewhat greater than it would have been in the case when the thermocline is forced remotely from the western Pacific. For the chosen meridional wind stress anomaly the effective offshore decay scale reaches about 40° at 25°N . At about 10°N , this offshore decay scale is even longer (due to a faster Rossby wave speed) so that the response to the coastal forcing extends as far as the basin western boundary.

We have compared the offshore decay scales given by the $1\frac{1}{2}$ -layer model and the low-frequency approximation (Figure 6b, solid and dashed lines respectively) and the two models agree well except for shorter oscillation periods. It is also important that the effect of the coastal wind stress is felt along the coast farther north of the region where the wind stress anomaly is applied. This is a consequence of ocean adjustment along the coast (the thermocline depth farther north should match that in the region where the wind stress changes).

4.3 Mid-latitude meridional wind stress

Finally, we apply a wind stress anomaly of the same shape as previously but now located offshore ($\tau(y) = Ae^{-\alpha(y-y_c)^2} e^{-\gamma(x-x_c)^2} e^{i\omega t}$ with $\tau(x) = 0$). In the next examples, the wind stress anomaly is centered at 25°N , the forcing period is set to 10 years, and we change the value of x_c to move the anomaly progressively away from the eastern boundary ($x_c=260^\circ\text{E}$, 240°E and 200°E , see Figure 12, left column). The results from equation (25) are shown in Figure 12 (middle column) representing thermocline depth anomalies at the instance when the wind stress is directed northward.

Ekman transport causes a deepening of the thermocline to the east and a shoaling to the west of the center of the wind stress anomaly, which creates a dipole-like anomaly of the thermocline depth. It is significant that the effect of the applied wind stress is felt far away from the wind anomaly itself. We again compare these results to the $1\frac{1}{2}$ -layer model (Figure 12, right column) and find a nearly perfect agreement.

As was done with the zonal mid-latitude wind stress case, we investigate the effect of the applied wind stress anomaly along the eastern boundary, but now at the latitude of the maximum wind stress, not at the equator (Figure 8b). As expected, the maximum response occurs when the wind stress anomaly is centered on the eastern boundary, with a constant thermocline anomaly depth of approximately six meters, which does not depend on the oscillation period. From Figure 12, we can also see that the maximum thermocline depth anomaly occurs in the same area as the applied wind stress anomaly, and decreases away from the wind stress. As the wind stress is moved offshore, the effect at the eastern boundary decreases to nearly zero when the winds are centered 40° away from the coast.

Comparing Figures 8a and b suggests that ocean response off the coast of California to remote winds (that is, zonal winds in the western equatorial Pacific) is significantly stronger than its response to local alongshore winds. This agrees with observational results of Dottori and Clarke (2009).

5 Conclusion

We have used the low-frequency approximation to describe the response of the ocean thermocline to wind variations over the Pacific Ocean on interannual to decadal timescales. Following this approach, we have expanded solutions of the shallow water equations in powers of the small parameter $\varepsilon = \varepsilon_m + i\omega$ and formally derived leading-order analytical expressions for thermocline anomalies induced by wind stress variations of arbitrary shape (ω and ε_m are nondimensional oscillation frequency and oceanic damping rate, respectively). We have applied these results to several particular examples, including variations in zonal equatorial winds in the western Pacific, coastal meridional winds over the California Current system, and mid-latitude winds. The first two cases are relevant to ENSO and its remote effects (i.e. teleconnections), whereas the third case is relevant for decadal climate variability in the Pacific.

A comparison of the low-frequency limit to the full solutions of the reduced-gravity shallow-water equations within the 1½-layer model indicates a good quantitative accuracy of our approach for oscillation periods longer than 2 years. We see good agreement in both the magnitude of generated thermocline anomalies and their spatial structure. For shorter oscillation periods our results still demonstrate a good qualitative agreement with the shallow-water solutions.

The main advantage of the low-frequency approach is that it provides simple explicit expressions for thermocline anomalies and a variety of other characteristics of the ocean response to oscillating winds. For instance, the low-frequency approximation gives explicitly the offshore decay scale of thermocline anomalies near the eastern boundary.

When forced by a zonal wind stress anomaly in the western equatorial Pacific, thermocline anomalies at the basin eastern boundary extend offshore to a distance inversely proportional to $y^2 \varepsilon_m$, where y is latitude. This scale is controlled by the gradual damping of Rossby waves generated at the coastline.

Similar analysis of the offshore decay scale of thermocline anomalies forced by local meridional wind stress along the eastern boundary shows dependence both on Rossby wave propagation and the structure of the wind stress anomalies themselves.

Another result from the low-frequency approach is a simple expression for ϕ – the phase lag between variations in the mean thermocline depth along the equator and the Niño3 SST. The latter typically lags the former by 4 months to a year. This lag is an important element of the recharge models of ENSO. The derived expression depends on the oscillation frequency and the spatial structure of wind anomalies, in particular the meridional shape of the anomalies α and the location of their maximum with respect to the equator y_c . Even a 2-3° shift in the location of the maximum can result in large changes of the lag. This has far-reaching implications for the behavior of coupled

climate models, which often generate wind anomalies not entirely symmetric with respect to the equator.

In summary, the low-frequency approximation is a useful tool for modeling ENSO and decadal climate variability in the Pacific, describing ocean response to idealized oscillatory wind variations (zonal or meridional), and providing an alternative to solving the traditional shallow-water equations. With a few minor modifications the method can be applied for modeling other equatorial basins as well. The method can also be used for non-sinusoidal wind stress variations as long as the wind forcing has a spectrum dominated by low frequencies. Finally, it can be easily generalized for the case when the key parameters of the problem (e.g. the mean thermocline depth or oceanic damping rate) vary as a function of latitude and longitude.

Acknowledgement

This research was supported in part by grants from NSF (OCE-0901921) and Department of Energy Office of Science (DE-FG02-08ER64590).

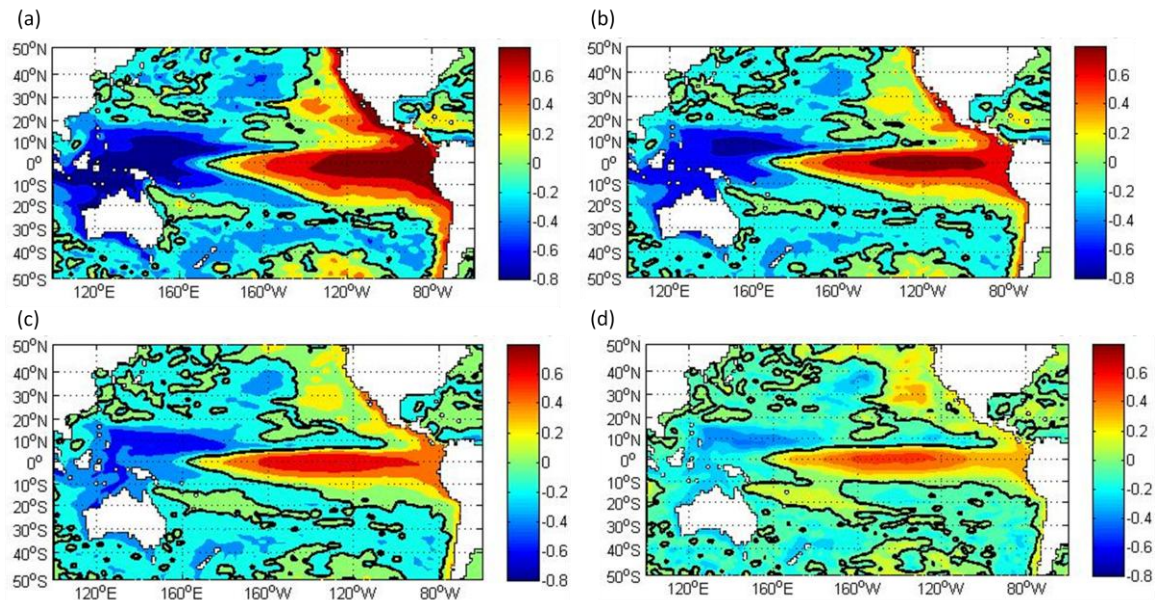


Figure 1 Lagged point-correlation maps between sea surface height anomalies (SSH) and the Niño3 SST index. (a), (b), (c), and (d): SSH lags SST by 0, 2, 4, and 6 months, respectively. In effect, these maps show the structure of SSH anomalies during and after the peak of an El Niño event. Note the extension of the El Niño signal along the west coast of the Americas. SSH is a proxy for the local thermocline depth. SSH data are from AVISO (<http://www.aviso.oceanobs.com>), SST data are from NOAA Climate Prediction Center (<http://www.cpc.noaa.gov/data/indices>), for the period December 1992 – December 2008.

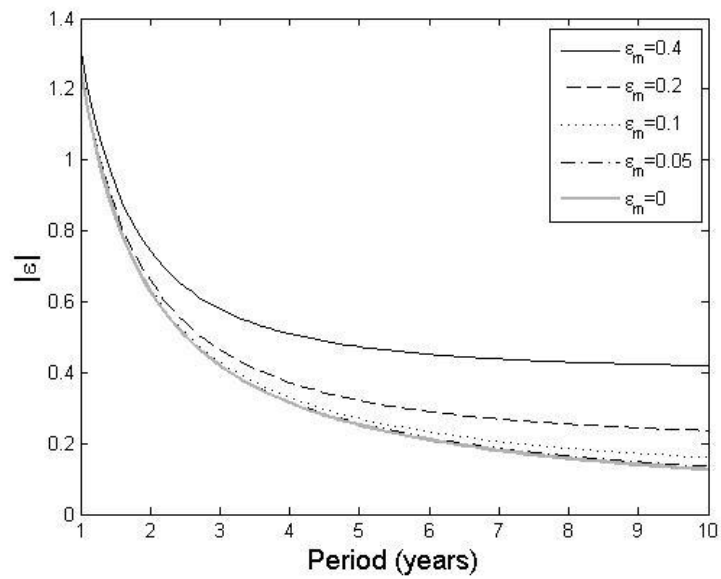


Figure 2 The absolute value of the nondimensional expansion parameter $\varepsilon = \varepsilon_m + i\omega$ as a function of oscillation period for different damping rates ε_m . For periods longer than approximately 2.5 years and realistic choices of ε_m , the value of $|\varepsilon|$ is smaller than 0.5.

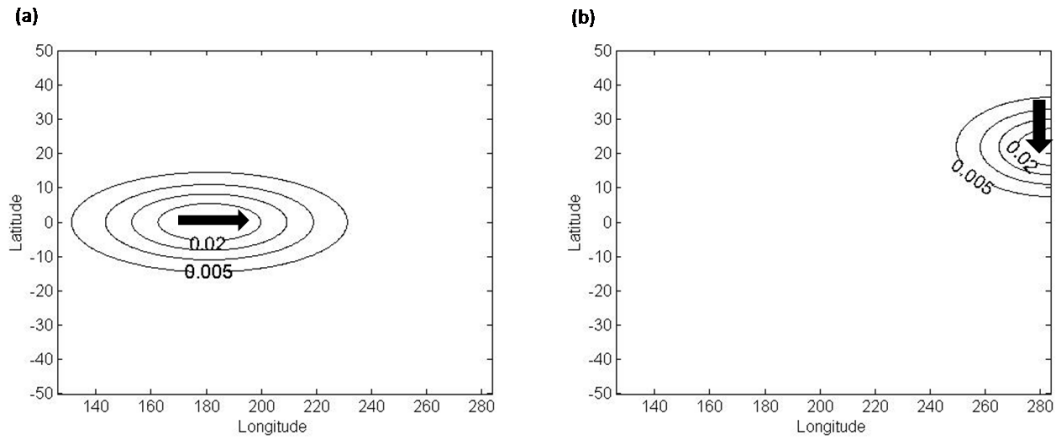


Figure 3 The shape of (a) zonal and (b) meridional wind stress anomalies (in N/m^2) that we apply along the equator and along the eastern boundary of the basin, respectively. The arrows indicate wind direction during one phase of the oscillation.

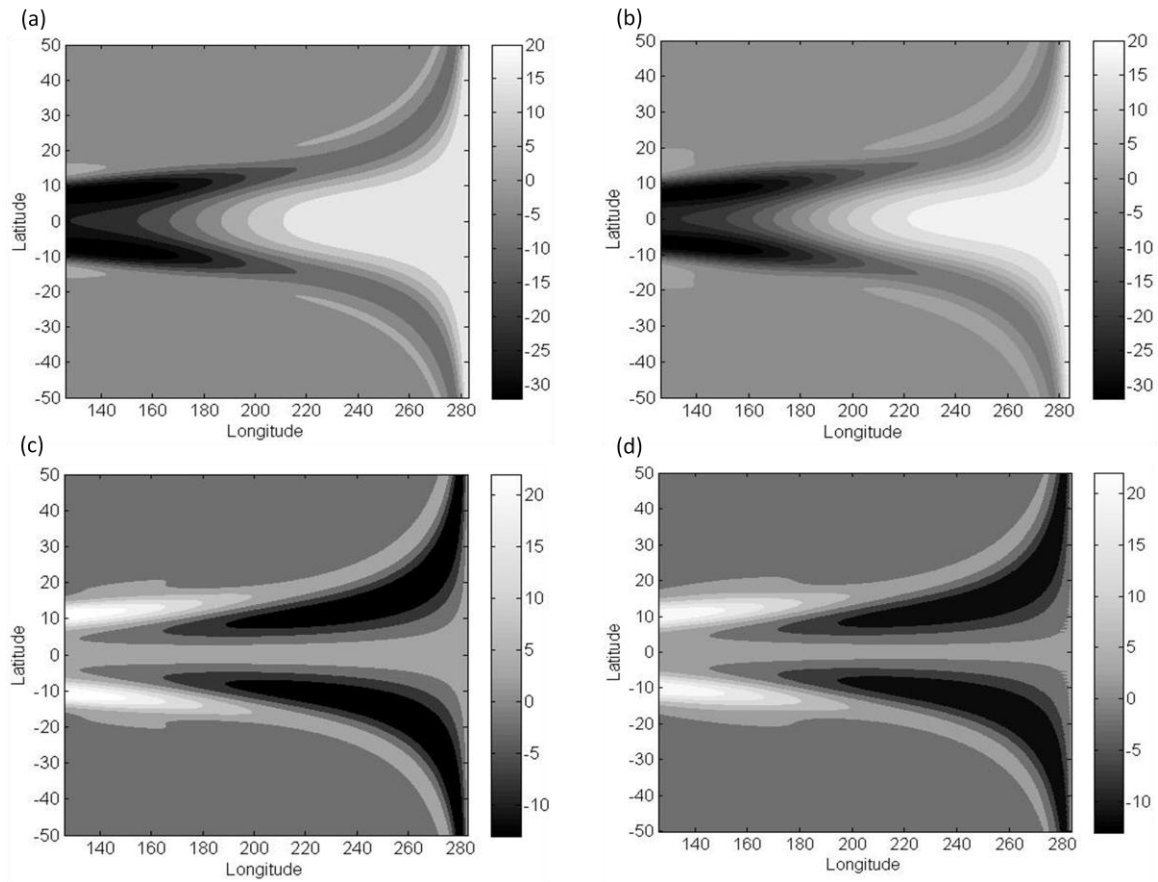


Figure 4 Thermocline depth anomalies forced by a zonal sinusoidal wind stress anomaly with a period of 4 years applied along the equator in the Pacific. Left panels: from equation (16) of the low-frequency approximation. Right panels: from the $1\frac{1}{2}$ -layer shallow-water model. Black and white colors indicate shoaling and deepening of the thermocline, respectively. Anomalies in (a) and (b) correspond to an El Niño event. Anomalies in (c) and (d) would occur one quarter-period prior to that.

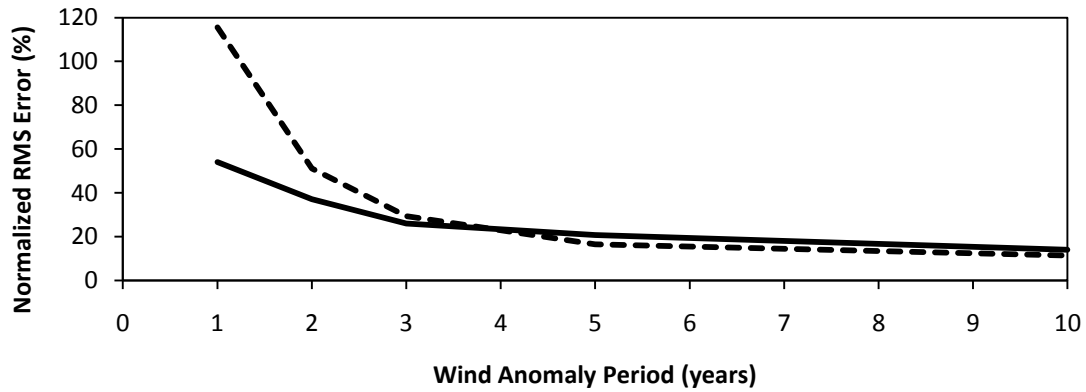


Figure 5 Normalized root mean squared difference $\left(\left[\int \int (h_{1.5} - h_{lf})^2 dx dy \right]^{1/2} \left[\int \int (h_{1.5})^2 dx dy \right]^{-1/2} \right)$ calculated between 50°N and 50°S for the 1½-layer model and low-frequency results for experiments with zonal equatorial (solid line) and coastal meridional (dashed line) wind stress anomalies and different periods of the forcing. The difference is calculated when the wind stress is maximum. The low-frequency limit works best for interannual and decadal timescales.

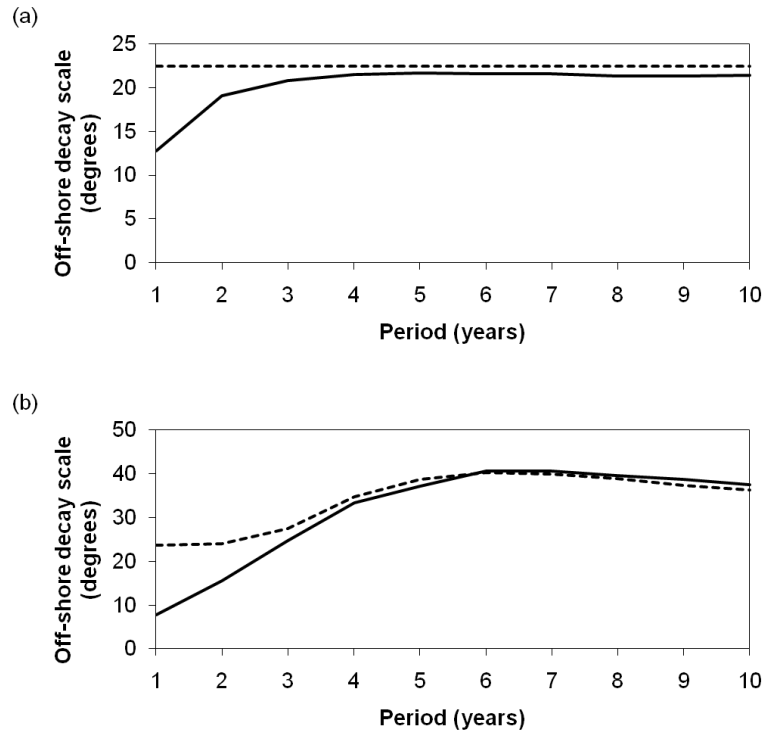


Figure 6 The e-folding offshore decay scale of thermocline depth anomalies near the basin eastern boundary at around 25°N as a function of the oscillation period as calculated from the $1\frac{1}{2}$ -layer model (solid line) and the low-frequency results from equation (18) (dashed line). The imposed forcing is zonal equatorial wind stress anomalies in the western Pacific in (a) and meridional wind stress anomalies along the basin eastern boundary in (b), (c.f. Figures 4 and 11).

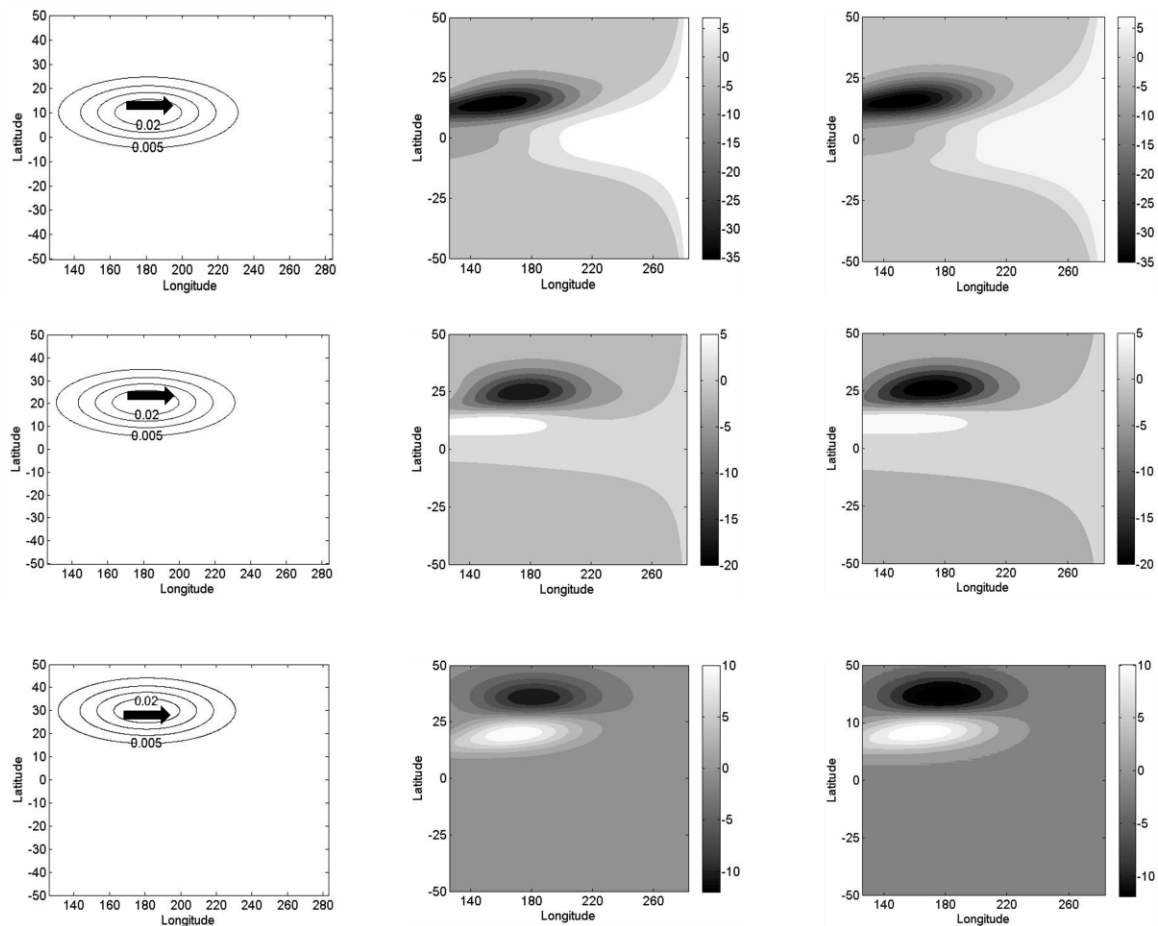


Figure 7 (Left column) The shape of applied zonal wind stress anomalies (in N/m^2) centered at different latitudes. From top to bottom: $y_c=10^\circ\text{N}$, 20°N and 30°N . The oscillation period is 10 years. (Middle and right columns) Resulting thermocline depth anomalies (in meters) calculated from equation (16) of the low-frequency approximation and from the $1\frac{1}{2}$ -layer model, respectively, at the instance when the wind stress is maximum. Black and white colors indicate shoaling and deepening of the thermocline, respectively. The main effects of the wind stress is to deepen the thermocline to the south and shoal it to the north of the wind anomaly. For $y_c=10^\circ\text{N}$, the overall thermocline response still resembles that during El Niño but is skewed towards the northern hemisphere.

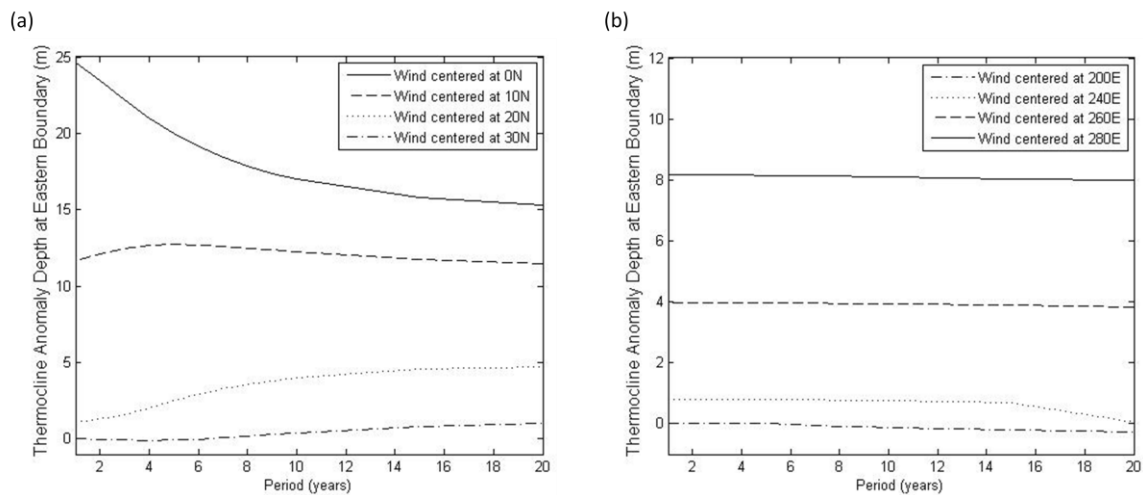


Figure 8 The amplitude of the thermocline depth anomaly at the basin eastern boundary for different wind stress anomalies of realistic strength and different oscillation periods. (a) Thermocline response to zonal wind stress anomalies centered at 0°N, 10°N, 20°N and 30°N (as in Figure 7). Note that in these cases the thermocline depth at the eastern boundary does not depend on latitude. (b) Thermocline response at 25°N to meridional wind stress anomalies centered at 280°E, 260°E, 240°E and 200°E (c.f. Figure 12).

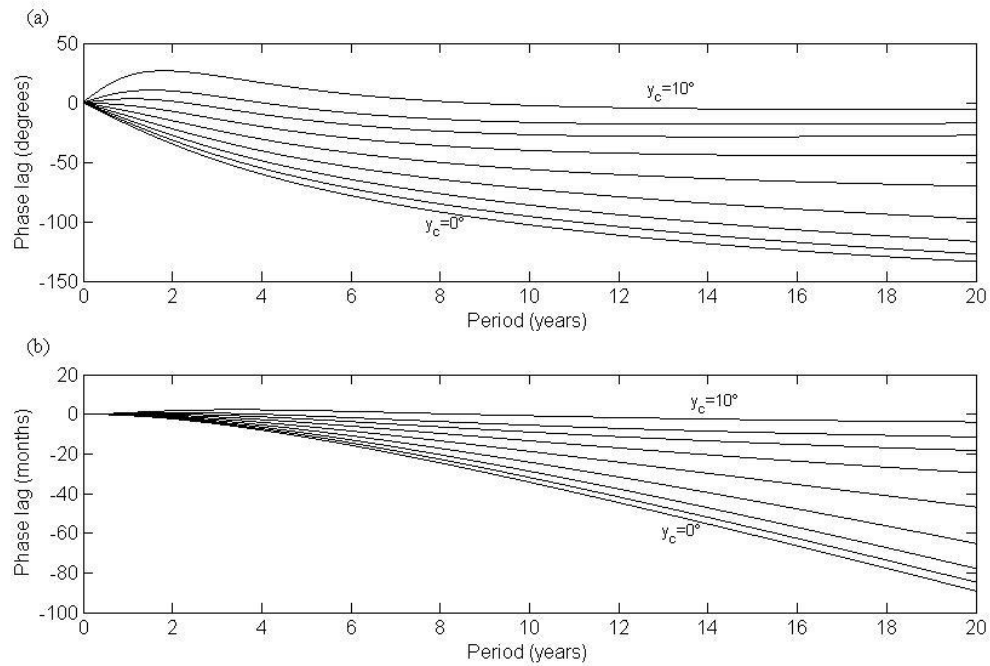


Figure 9 Phase lag between the eastern equatorial SST (T_e) and the mean equatorial thermocline depth (h_m) in (a) degrees and (b) months as a function of the oscillation period for different locations of wind stress anomalies with respect to the equator (y_c). Negative phase lag indicates that T_e lags h_m . Each line corresponds to a different y_c ; from top to bottom y_c varies from 10° to 0° N with a 1° increment. For all calculations $\alpha=0.12$, $\epsilon_m=0.1$.

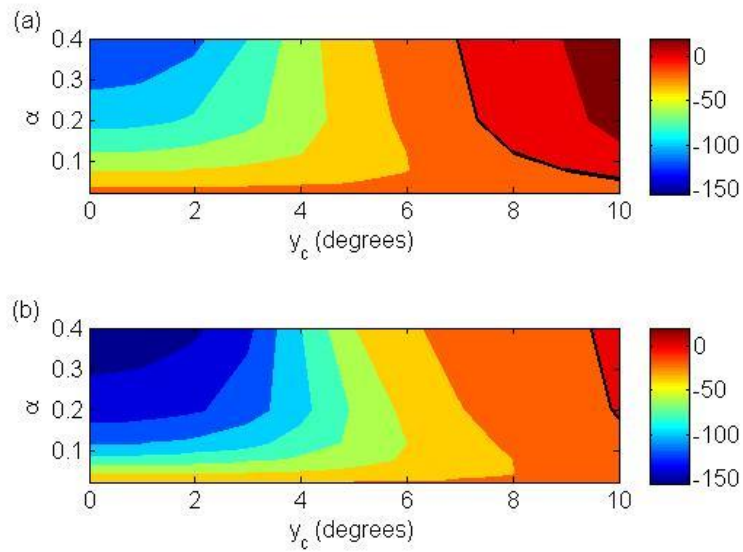


Figure 10 Phase lag (in degrees) between the eastern equatorial SST (T_e) and the mean equatorial thermocline depth (h_m) as a function of α and y_c for two oscillation periods P : (a) $P=4$ years. (b) $P=10$ years. Negative phase lag values indicate that T_e lags h_m . The zero contour is denoted by a solid black line.

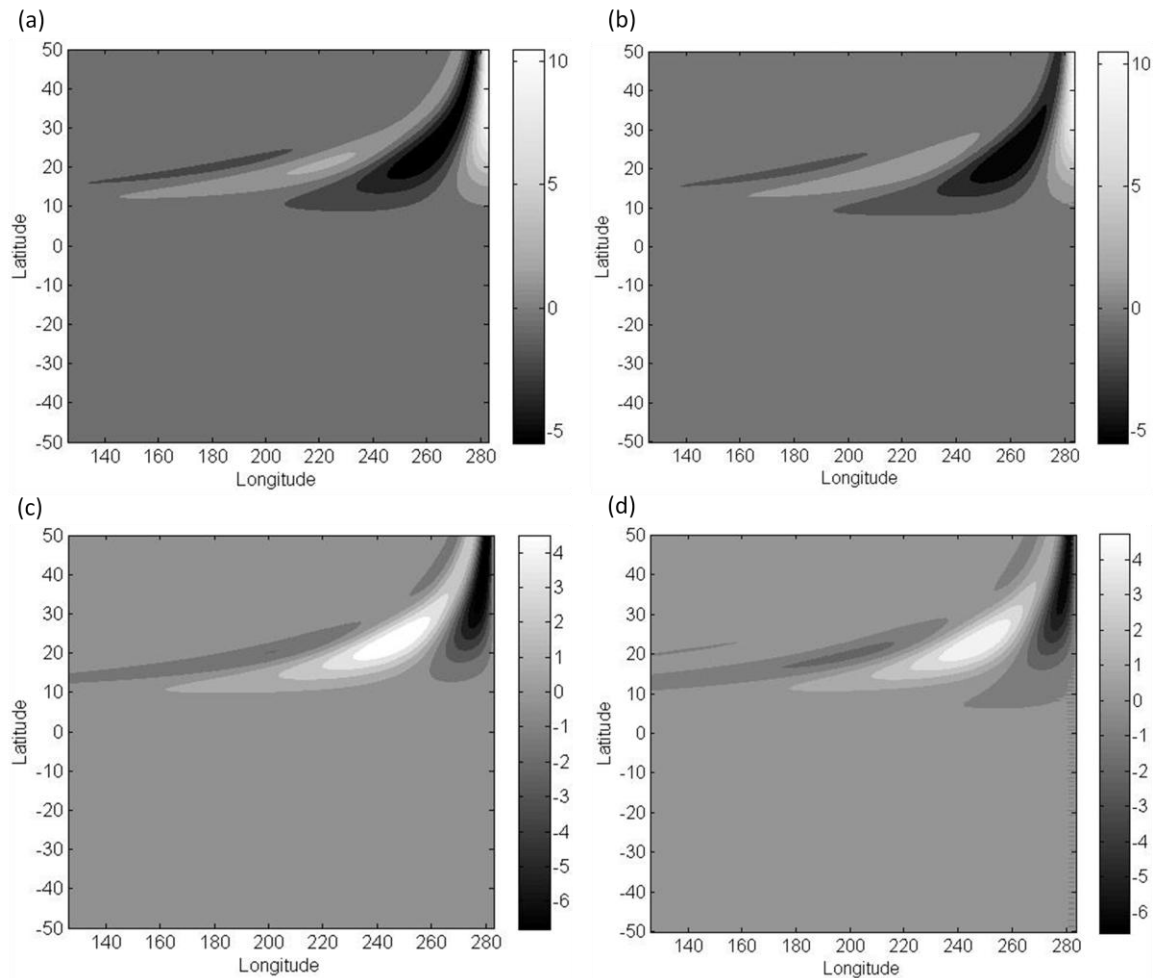


Figure 11 Thermocline depth anomalies forced by meridional wind stress anomalies with a period of 4 years centered at the basin eastern boundary, see Figure 3. (a) and (c) as calculated from equation (25) of the low-frequency limit; (b) and (d) as obtained from the 1½-layer model. Black and white colors indicate shoaling and deepening of the thermocline, respectively. Panels of the top row show ocean response when the wind stress anomaly is maximum and northward. Panels of the bottom row show the ocean state a quarter-period prior to that. Note that thermocline anomalies extend far north and west of the wind stress anomaly.

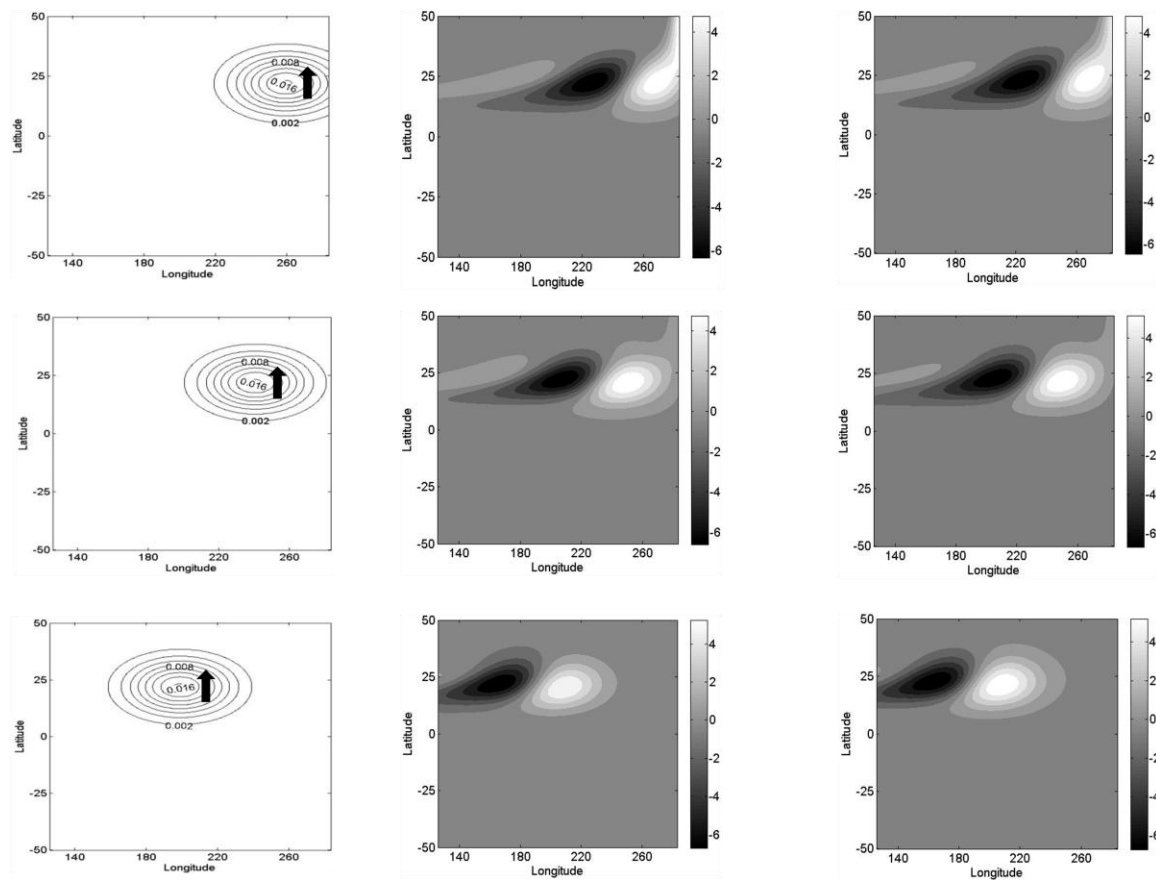


Figure 12 (Left column) The shape of applied meridional wind stress anomalies (in N/m^2) each centered at 25°N but different longitudes. The oscillation period is 10 years. From top to bottom: $x_c=260^\circ\text{E}$, 240°E and 200°E . (Middle and right columns) Resulting thermocline depth anomalies (in meters) calculated from equation (16) of the low-frequency approximation and from the $1\frac{1}{2}$ -layer model, respectively, at the instance when the wind stress is maximum. Black and white colors indicate shoaling and deepening of the thermocline, respectively. The main effect of the wind stress is to deepen the thermocline to the east and shoal it to the west of the wind stress anomaly. Note that thermocline anomalies extend far west of the wind anomaly. For $x_c=260^\circ\text{E}$, the effect of the wind is still felt along the coast.

References

- Battisti, David S., 1998. Dynamics and thermodynamics of a warming event in a coupled tropical atmosphere-ocean model. *J. Atmos. Sci.*, 45:2889-2919.
- Clarke, A.J., 2010. Analytical theory for the quasi-steady and low-frequency equatorial ocean response to wind forcing: The 'tilt' and 'warm water volume' modes. *J. Phys. Oceanogr.*, 40:121-137.
- Clarke, A. J., and M. Dottori, 2008. Planetary wave propagation off California and its effect on zooplankton. *J. Phys. Oceanogr.*, 38(3):701-713.
- Deser, Clara, Michael A. Alexander, and Michael S. Timlin, 1996. Upper-ocean thermal variations in the North Pacific during 1970-1991. *J. Clim.*, 9:1840-1855.
- Di Lorenzo E., Schneider N., Cobb K. M., Chhak, K, Franks P. J. S., Miller A. J., McWilliams J. C., Bograd S. J., Arango H., Curchister E., Powell T. M. and P. Rivere, 2008. North Pacific Gyre Oscillation links ocean climate and ecosystem change. *Geophys. Res. Lett.*, 35:L08607.
- Dottori, M., and Clarke, A.J., 2009. Rossby waves and the interannual and interdecadal variability of temperature and salinity off California. *J. Phys. Oceanogr.*, 39:2543-2561.
- Emile-Geay, Julien and Mark A. Cane, 2009. Pacific decadal variability in the view of linear equatorial wave theory. *J. Phys. Oceanogr.*, 39:203-219.
- Enriquez, A.G. and C.A. Friehe, 1995. Effects of wind stress and wind stress curl variability on coastal upwelling. *J. Phys. Oceanogr.*, 25:1651-1671.
- Fedorov, A.V., 2010. Ocean response to wind variations, the equatorial warm water volume, and simple models of ENSO: the low-frequency approximation. *J. Climate*, 23:3855-3873.
- Fedorov, A.V. and Brown, J. 2009. Equatorial Waves. *Encyclopedia of Ocean Sciences*, J. Steele, Ed., Academic Press, 3679-3695.
- Jacobs, G.A., H.E. Hurlburt, J.C. Kindle, E.J. Metzger, J.L. Mitchell, W.J. Teague and A.J. Wallcraft, 1994. Decade-scale trans-Pacific propagation and warming effects of an El Niño anomaly. *Nature*, 370:360-363.
- Jin, F.-F., 1997. An equatorial ocean recharge paradigm for ENSO. Part I: Conceptual model. *J. Atmos. Sci.*, 54:811-829.
- Jin, F.-F. and J. David Neelin, 1993. Modes of interannual tropical ocean-atmosphere

- interaction - A unified view. Part I: Numerical results. *J. Atmos. Sci.*, 50:3477-3503.
- Hare, Steven R. and Nathan J. Mantua, 2000. Empirical evidence for North Pacific regime shifts in 1977 and 1989. *Prog. Oceanogr.*, 47:103-145.
- Hermann, Albert J., Enrique N. Curchitser, Dale B. Haidvogel, and Elizabeth L. Dobbins, 2009. A comparison of remote vs. local influence of El Niño on the coastal circulation of the northeast Pacific. *Deep-Sea Research II*, 56:2427-2443.
- Huyer, A., R.L. Smith, and J. Fleishbein, 2002. The coastal ocean off Oregon and northern California during the 1997-8 El Niño. *Prog. in Oceanogr.*, 54:311-341.
- Jacobs, G.A., H.E. Hurlburt, J.C. Kindle, E. J. Metzger, J.L. Mitchell, W.J. Teague, and A.J. Wallcraft, 1994. Decade-scale trans-Pacific propagation and warming effects of an El Niño anomaly. *Nature*, 370:360-363.
- Lluch-Cota, Daniel B., Warren S. Wooster, Steven R. Hare, Daniel Lluch-Belda, and Alejandro Parés-Sierra, 2003. Principle Modes and Related Frequencies of Sea Surface Temperature Variability in the Pacific Coast of North America. *J. Oceanogr.*, 59:477-488.
- Mantua, Nathan J. and Steven R. Hare, 2002. The Pacific Decadal Oscillation. *J. Oceanogr.*, 58:35-44.
- Meinen, C.S. and M.J. McPhaden, 2000. Observations of warm water volume changes in the equatorial Pacific and their relationship to El Niño and La Niña. *J. Climate*, 13:3551-3559.
- Meyers, S.D., M.A. Johnson, M. Liu, J.J. O'Brien, and J.L. Spiesberger, 1996. Interdecadal variability in a numerical model of the northeast Pacific ocean: 1970-89. *J. Phys. Oceanogr.*, 26:2635-2652.
- Miller, A.J. et al., 1999. Observing and modeling the California Current System. *Eos, Transactions, AGU*, 80:533-539.
- Nitta, Tsuyoshi and Shingo Yamada, 1989. Recent warming of tropical sea surface temperature and its relationship to the Northern Hemisphere circulation. *J. Met. Soc. Japan*, 67:375-383.
- Pares-Sierra, A. and J.J. O'Brien, 1989. The seasonal and interannual variability of the California Current System: a numerical model. *J. Geophys. Res.*, 94:3159-3180.
- Parrish, R. H., R.B. Schwing, and R. Mendelsohn, 2000. Mid-latitude wind stress: the energy source for climatic shifts in the North Pacific Ocean. *Fish. Oceanogr.*, 9:224-238.

- Philander, S. George, 1990. *El Niño, La Niña, and the Southern Oscillation*. Academic Press, California.
- Schwing, F.B., T. Murphee, L. deWitt and P.M. Green, 2002. The evolution of oceanic and atmospheric anomalies in the northeast Pacific during the El Niño and La Niña events of 1995-2001. *Prog. In Oceanog.*, 54:459-491.
- Strub, P.T. and C. James, 2002. The 1997-1998 El Niño signal along the southeast and northeast Pacific boundaries – an altimetric view. *Prog. in Oceanog.*, 54:439-458.
- Subbotina, Marina M., Richard E. Thomson, and Alexander B. Rabinovich, 2001. Spectral characteristics of sea level variability along the west coast of North America during the 1982-83 and 1997-98 El Niño events. *Prog. in Oceanog.*, 49:353-372.